

## Collisionless Shock Acceleration of High-Flux Quasimonoenergetic Proton Beams Driven by Circularly Polarized Laser Pulses

H. Zhang,<sup>1</sup> B. F. Shen,<sup>1,2,3,\*</sup> W. P. Wang,<sup>1</sup> S. H. Zhai,<sup>1</sup> S. S. Li,<sup>1</sup> X. M. Lu,<sup>1</sup> J. F. Li,<sup>1</sup> R. J. Xu,<sup>1</sup>  
X. L. Wang,<sup>1</sup> X. Y. Liang,<sup>1</sup> Y. X. Leng,<sup>1</sup> R. X. Li,<sup>1,3,†</sup> and Z. Z. Xu<sup>1,3</sup>

<sup>1</sup>State Key Laboratory of High Field Laser Physics, Shanghai Institute of Optics and Fine Mechanics,  
Chinese Academy of Sciences, Shanghai 201800, China

<sup>2</sup>Department of Physics, Shanghai Normal University, Shanghai 200234, China

<sup>3</sup>Collaborative Innovation Center of IFSA, Shanghai Jiao Tong University, Shanghai 200240, China

(Received 10 May 2017; published 17 October 2017)

We present experimental studies on ion acceleration using an 800-nm circularly polarized laser pulse with a peak intensity of  $6.9 \times 10^{19}$  W/cm<sup>2</sup> interacting with an overdense plasma that is produced by a laser prepulse ionizing an initially ultrathin plastic foil. The proton spectra exhibit spectral peaks at energies up to 9 MeV with energy spreads of 30% and fluxes as high as  $3 \times 10^{12}$  protons/MeV/sr. Two-dimensional particle-in-cell simulations reveal that collisionless shocks are efficiently launched by circularly polarized lasers in exploded plasmas, resulting in the acceleration of quasimonoenergetic proton beams. Furthermore, this scheme predicts the generation of quasimonoenergetic proton beams with peak energies of approximately 150 MeV using current laser technology, representing a significant step toward applications such as proton therapy.

DOI: 10.1103/PhysRevLett.119.164801

Laser-driven ion acceleration [1,2] is attracting widespread interest because of the prospects of realizing compact and affordable ion sources for many exciting applications [3] including cancer therapy, proton radiography, and inertial confinement fusion. Many of these applications require high-energy ion beams with narrow energy spread as well as high flux. Up until now, the relatively well-understood mechanism of laser-driven ion acceleration is target normal sheath acceleration (TNSA), which typically produces broad exponential energy spectra with a maximum proton energy of 85 MeV [4]. The possibility of generating quasimonoenergetic ion beams with the TNSA regime has been demonstrated by applying a small hydrogen-rich dot on the rear surface [5] or by resistive heating to remove contaminants [6]; however, ion energies are limited to a few megaelectronvolts with fluxes of approximately  $10^{10}$  ions/MeV/sr. Regarding applications, not only narrow energy spread but also high flux is important. Spectral selection from a TNSA exponential spectrum can cut out a narrow peak rather than enhance the particle flux. Compared to TNSA, the radiation pressure acceleration (RPA) process is known to have the potential to accelerate monoenergetic ion beams [7–10], where the whole laser-irradiated volume of an ultrathin solid target is propelled in unison by the radiation pressure in the “light-sail” model [11]. However, experimental evidence for RPA [12,13] is scant because of the extreme laser conditions required, such as ultrahigh laser contrast.

Recently, shock ion acceleration [14–19] has been proposed as an alternative method for the acceleration of high-quality ion beams. When an overdense target is irradiated by a laser pulse, ions are compressed to form a density spike, which in turn launches electrostatic shocks [20,21]. These shocks can reflect upstream ions and yield ion beams with

monoenergetic peaks as the shock Mach number exceeds the critical value ( $>1.5$ ). Another scheme of shock acceleration is based on the nonlinear threshold phenomenon of ion reflection from the front of the laser pulse, which can be applied for producing high-density quasimonoenergetic protons by focusing two counterpropagating laser pulses of relativistic intensities onto ultrathin nanolayers [22]. In recent experiments, the mechanism of shock acceleration has been demonstrated using CO<sub>2</sub> laser pulses of 10  $\mu$ m in wavelength interacting with high-density gas jets [23–25]. By using the circularly polarized (CP) laser, Palmer *et al.* reported 1-MeV protons with a 4% energy spread and a flux of  $4 \times 10^{11}$  protons/MeV/sr [23], where the hole-boring acceleration (HBA) is dominated and the shock is driven by the radiation pressure. When the linearly polarized (LP) laser is used, Haberberger *et al.* reported 20 MeV protons with a 1% energy spread and a flux of about  $10^7$  protons/MeV/sr [25], where the collisionless shock acceleration (CSA) becomes dominated and the shock is driven by the thermal pressure. Another route of shock ion acceleration has also been discovered by employing exploded targets and intense femtosecond laser pulses with a wavelength of 800 nm [16,26,27]. Here, overdense plasmas suitable for shock acceleration are produced by low-intensity lasers or prepulses heating and ionizing ultrathin solid targets. This method facilitates the enhancement of ion energy as femtosecond lasers can provide higher intensities than CO<sub>2</sub> lasers. Experimental data indicating signatures of the shock ion acceleration driven by short-wavelength lasers have been reported [26–28], but no sharp energy peak has been observed.

In this study, we experimentally demonstrate the generation of quasimonoenergetic proton beams by using

800-nm, CP laser pulses interacting with exploded targets. A proton beam with an energy of 9 MeV, energy spread of 30%, and high flux of  $3 \times 10^{12}$  protons/MeV/sr is generated. Two-dimensional (2D) particle-in-cell (PIC) simulations matching the experimental parameters reproduce the observed proton spectra and demonstrate that collisionless shocks are efficiently launched by CP lasers in overdense plasmas and facilitate the acceleration of narrow-energy-spread proton beams. Furthermore, this scheme predicts the generation of protons with peak energies of approximately 150 MeV using current laser technology. To be noted, when a LP laser is used, the proton spectrum almost monotonically decays, while the spectral peak is apparent only when viewing it in logarithmic coordinates [26].

The experiments were carried out using a Ti:sapphire chirped pulse amplification laser system [29], delivering an on-target energy of 13 J. The laser pulse with a full-width at half-maximum (FWHM) duration of 55 fs and central wavelength of 800 nm was focused by an  $f/4$  off-axis parabolic mirror onto a flat polyvinyl-formal target with a thickness of 40 nm at an angle of incidence of  $26^\circ$ . A peak intensity of  $6.9 \times 10^{19}$  W/cm<sup>2</sup> is achieved with a focal spot diameter (FWHM) of 14  $\mu$ m (containing about 45% laser energy). A mica crystal as a quarter-wave plate is used to change the laser from a linear to circular polarization. The peak normalized vector potential of the laser pulse is  $a_0 = 5.6$  and 4 for the linear and circular polarization, respectively. The high-contrast laser with a contrast ratio of about  $10^{11}$  at 60 ps before the main pulse peak was achieved through noncollinear optical parametric amplification and second-harmonic generation processes [30,31]. Here, the plasma mirror is not introduced into the laser beam path; thus, the laser prepulse is sufficiently intense to induce the premature ionization and expansion of the targets, especially nanometer-thick ultrathin foils.

A schematic of the experimental setup is shown in Fig. 1(a). Radiochromic film stacks are positioned 7 cm behind the rear of the target to record the ion-beam divergence. To detect the spectra of the forward-propagating ions, a Thomson parabola (TP) spectrometer is placed 46 cm (solid angle  $\sim 9.2 \times 10^{-9}$  sr) away from the target along the normal direction. Ion traces are recorded by BAS-TR image plates (IPs) attached to the back side of the TP spectrometer [31]. In addition, a magnetic electron spectrometer (ES) equipped with BAS-SR IPs is positioned at an angle of  $16^\circ$  with respect to the target normal direction to measure the electron spectra.

In Figs. 1(b)–1(c), we present the raw IP data of the TP spectrometer and ES from 40-nm plastic foils irradiated by the CP and LP laser pulses with a peak intensity of  $6.9 \times 10^{19}$  W/cm<sup>2</sup>. An isolated quasimonoenergetic feature of protons located in the 4.5 to 14 MeV energy region is observed for the CP laser, whereas for the LP laser, the signal intensity of protons possesses no distinct fluctuation in the 4.5 to 10 MeV energy region. The corresponding

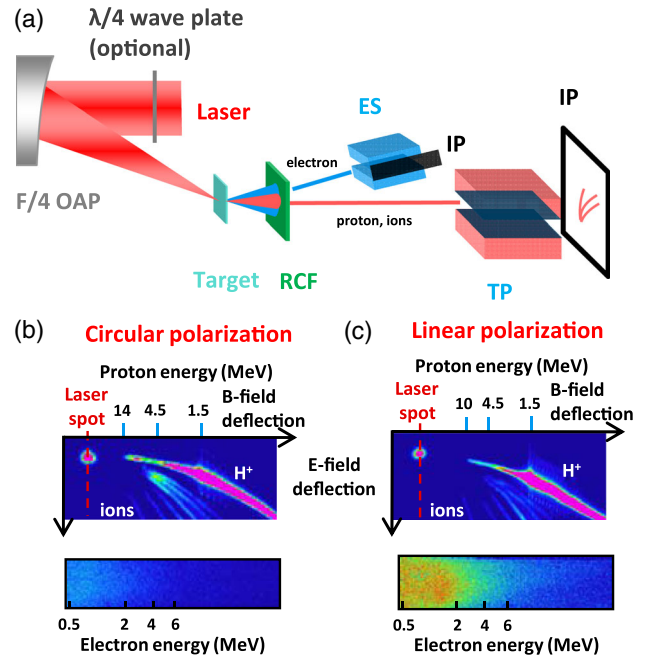


FIG. 1. (a) Schematic of the experimental setup. Image plate data of Thomson parabola and electron spectrometer obtained from 40-nm plastic foils irradiated by (b) CP and (c) LP laser pulses with a peak intensity of  $6.9 \times 10^{19}$  W/cm<sup>2</sup>.

proton spectra are plotted in Fig. 2(a). A monotonically decaying spectrum with a cutoff energy of 10 MeV is obtained for the LP laser. In contrast, when the laser beam is changed to a circular polarization, the proton spectrum exhibits a well-defined spectral peak at 9 MeV with an energy spread (FWHM) of 30% and flux of  $3 \times 10^{12}$  protons/MeV/sr. This flux is at least two orders of magnitude greater than the previously reported results from the TNSA mechanism [5]. The conversion efficiency from laser to protons within a peak energy interval of 6 to 12 MeV is estimated at about 1% (assuming a beam with divergence half-angle of  $3^\circ$ ), which is much higher than that obtained with the HBA and CSA regime driven by CO<sub>2</sub> lasers [23–25]. The carbon spectra for both CP and LP cases exponentially decay (see the Supplemental Material [31] for more information). The maximum energy of the carbon ions for the CP case is 1.7 MeV/nucleon, which is much smaller than the lower threshold of the spectral peak of protons (about 5 MeV). This scenario is contrary to our previous results because of the use of different laser and target parameters [26]. Figure 2(b) shows the processed electron spectra. It can be clearly seen that the CP laser results in a reduction of electron heating, which is consistent with the simulation, as will be explained later.

The spectral peak of the protons is repeatedly observed for the CP laser. The proton spectra of the three different laser shots with lower intensities of  $2.7 \times 10^{19}$ ,  $3.6 \times 10^{19}$ , and  $5.5 \times 10^{19}$  W/cm<sup>2</sup> are presented in Fig. 2(c). All these spectra exhibit spectral peaks, but the peak energies vary

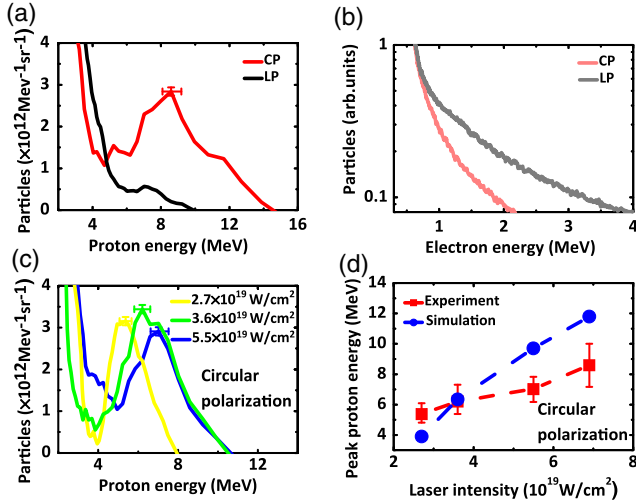


FIG. 2. Processed energy spectra of (a) protons and (b) electrons in the case of CP (red, light red lines) and LP (black, gray lines) laser pulses with a peak intensity of  $6.9 \times 10^{19}$  W/cm<sup>2</sup> irradiating 40-nm plastic foils. (c) Details of proton spectra for CP laser with intensities of  $2.7 \times 10^{19}$  (yellow line),  $3.6 \times 10^{19}$  (green line), and  $5.5 \times 10^{19}$  W/cm<sup>2</sup> (blue line). (d) Experimental (red squares) and simulated (blue circles) results of the peak energy of quasimonoenergetic protons as a function of laser intensity, where the vertical bars represent the FWHM energy spread of each shot.

between 5 and 7 MeV. The peak proton energy decreases with the decrease in laser intensity, which is shown more clearly in Fig. 2(d). This trend agrees with the simulated results, indicating that the shock velocity decreases when reducing the laser intensity. The vertical bars in Fig. 2(d) represent the FWHM energy spread of each shot, with a minimum of 20% at 5.4 MeV. Note that the proton flux has no significant change even when the laser intensity is reduced to  $2.7 \times 10^{19}$  W/cm<sup>2</sup>.

To understand the experimental results, 2D PIC simulations were performed to elucidate the mechanism of ion acceleration. A Gaussian laser pulse with a FWHM duration of 55 fs and FWHM focal spot diameter of  $14 \mu\text{m}$  was used, resulting in  $a_0 = 4$  for the CP laser and  $a_0 = 5.6$  for the LP laser. The size of the simulation box was  $200$  and  $160 \mu\text{m}$  in the longitudinal ( $x$ ) and transverse ( $y$ ) dimensions, respectively, divided into  $10000 \times 8000$  cells. Each cell was filled with 20 particles. The interaction of the laser prepulse with an initial plastic foil was simulated using one-dimensional hydrodynamic code [33,34]. The following formula, which adequately approximates the hydrocalculation, was used to model the density profile of the expanding plasma [34]:  $n_e(x) = 2n_{e,\text{max}} / \{1 + \exp[(2\zeta\theta(\zeta)/l_b) - (2\zeta\theta(-\zeta)/l_f)]\}$ . Here,  $\zeta = x - 0.5l_0$  and  $\theta(x)$  is the step function. The parameters  $n_{e,\text{max}}$ ,  $l_b$ ,  $l_f$ , and  $l_0$  represent the peak plasma density, back and front scale lengths of the density ramps, and initial foil thickness, respectively. An overdense plasma

with  $n_{e,\text{max}} = 4n_c$  and  $l_b = l_f = 2 \mu\text{m}$  is obtained from the expansion of the initially rectangular target with  $l_0 = 40 \text{ nm}$  and  $n_0 = 360n_c$ , where  $n_c$  is the critical density for 800-nm lasers. In the 2D PIC simulations, a density maximum is located at  $x = 100 \mu\text{m}$ , where the main laser is focused at an angle of incidence of  $26^\circ$ . The number ratio of  $C^{6+}$  ions and protons in the overdense plasma is 1:2, with a peak proton density  $n_{p,\text{max}} = 1n_c$ . In the following, the simulation times are given relative to  $t = 0$  when the laser pulse reaches the position of peak plasma density ( $x = 100 \mu\text{m}$ ).

In Fig. 3(a), the calculated proton spectra at 377 fs are compared for the CP (red line) and LP (blue line) lasers, which are obtained with a  $1 \mu\text{m}$  average over  $y$  centered at  $y = 0$ . The LP case exhibits a broad energy spectrum, whereas the CP case yields a spectral peak, which agrees well with the experimental result [Fig. 2(a)]. In the simulation, the quasimonoenergetic proton beam is accelerated to 12 MeV with an energy spread of 20%. This proton beam originates from the reflection of the expanding protons in the upstream plasma, as shown in Fig. 3(c), and gains a velocity equal to twice the shock velocity minus the

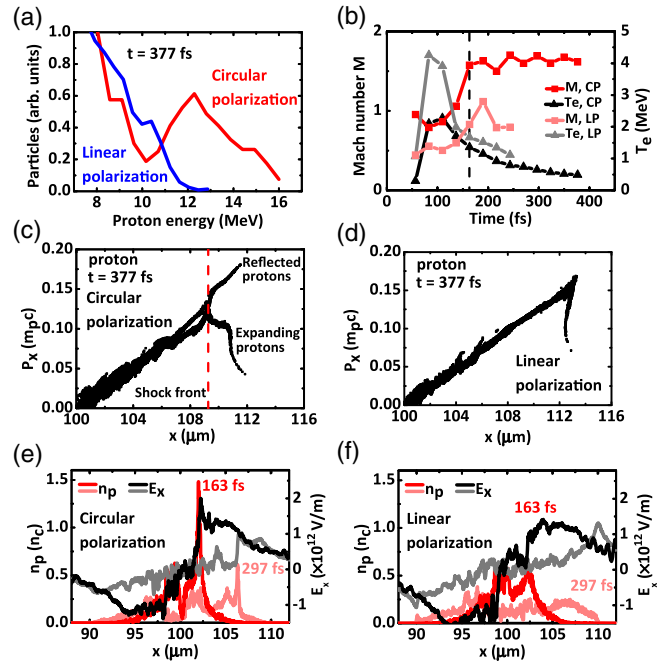


FIG. 3. Simulation results from CP laser of  $a_0 = 4$  and LP laser of  $a_0 = 5.6$  interacting with overdense plasmas of  $n_{e,\text{max}} = 4n_c$ . (a) Proton spectra for CP (red line) and LP (blue line) cases at 377 fs after the start of laser-plasma interaction. (b) Evolution of the Mach number (red, light red squares) with average electron temperature (black, gray triangles) in the upstream. The black dashed line represents the beginning of shock formation. (c)–(d) Corresponding proton phase spaces at 377 fs. (e)–(f) Longitudinal electric field  $E_x$  (red, light red lines) and transversely averaged proton density (black, gray lines) at two different times, 163 and 297 fs.

expanding velocity, thus proving the electrostatic shock being the dominant acceleration force. Here, the red dashed line represents the shock front. Shock ion acceleration driven by the CP lasers can also be verified by measuring the Mach number, given by  $M = v_s/c_s \sim 1.6$  [Fig. 3(b)], where  $v_s$  is the shock velocity in the upstream frame,  $c_s = \sqrt{ZkT_e/m_i}$  is the ion sound speed,  $kT_e$  is the electron temperature, and  $Z$  and  $m_i$  are the charge number and ion mass, respectively. This value satisfies the estimation of the Mach number of electrostatic shocks  $M > 1.5$  from Ref. [21]. For the CP case, the carbon ions are not reflected like the protons because of the smaller charge-to-mass ratio, leading to the monotonically decreasing spectrum which is consistent with the experimental result [31]. The maximum carbon velocity is much smaller than the peak velocity of the reflected protons, indicating that the acceleration of the quasimonoenergetic protons is not associated with the carbon acceleration. When the LP laser is used, these typical features of shock acceleration, including velocity doubling in phase space and a high Mach number, cannot be observed [Figs. 3(b) and 3(d)].

The striking difference of acceleration dynamics for the CP and LP lasers can be directly inferred by analyzing the electron temperature, plasma density, and longitudinal electric field, as observed in our simulations (Fig. 3). In the CP case, the protons are strongly compressed by the ponderomotive force of the CP laser. Therefore, a proton density spike with a high electrostatic potential energy is generated similar to a piston [Fig. 3(e)]. Meanwhile, the plasma electrons are inevitably heated up due to the oblique incidence of the pulse. The electron temperature in the upstream reaches the maximum at the end of the laser-plasma interaction ( $t = 110$  fs) and then decreases with the expansion of the plasma [Fig. 3(b)]. These electrons facilitate to launch the (thermal-pressure driven) collisionless shock wave, which can propagate in the exploded plasma for a long time even without the driving laser pulse [Fig. 3(e)]. As the potential energy of the shock is higher than the kinetic energy of the ions in the upstream, the Mach number of the shock reaches the critical value and reflection of the protons occurs at 163 fs. For the LP laser, the above scenario changes drastically. As shown in Fig. 3(b), the electrons are heavily heated at higher temperatures than that of the CP laser. Accordingly, these energetic electrons can easily escape from the density spike and the electric field is significantly reduced, resulting in a weak compression of proton density [Fig. 3(f)]. Though the LP case also yields a density spike, the potential is too weak to reflect protons with high sound speeds. Figure 3(f) indicates that the structure of the density spike and bipolar electric field disappears at 297 fs, revealing that the acceleration is dominated by the sheath field.

Compared with the (radiation-pressure driven) HBA and (thermal-pressure driven) CSA mechanisms demonstrated with CO<sub>2</sub> lasers, shock ion acceleration driven by an 800-nm

CP laser pulse at oblique incidence has some different features. On the one hand, reflection of the protons occurs after complete leaving of the laser pulse. This is a different feature from the HBA regime, where the protons are reflected during the laser-plasma interaction. On the other hand, considering that the time interval between the end of the laser-plasma interaction and reflection of the protons is short (53 fs) and especially the density profile of the exploded plasma is exponentially decaying, the shock structure can propagate in the plasma without significant momentum loss. As a consequence, the final shock velocity is closely associated with the initial piston velocity. This is different from the conventional CSA regime, where shock formation is not related to the laser piston action and for the case of Ref. [25] the final shock velocity is an order of magnitude higher than the initial piston velocity. Furthermore, the use of the oblique incidence of the laser leads to electron heating, which in turn induces the thermal pressure and finally contributes to formation of the collisionless shock wave. These results indicate that the use of the CP laser and oblique incidence of the pulse in our experiments lead to a hybrid regime between the HBA and CSA process where both the radiation and thermal pressures play an important role in the shock formation and proton acceleration.

Further simulations using CP lasers with a smaller  $a_0$  were performed, and all proton spectra exhibited spectral peaks (not shown here). When  $a_0$  was reduced from 3.6 to 2.5, the peak proton energy dropped from 10 to 4 MeV. This variation in energy agrees with the observed result in the experiment [Fig. 2(d)]. To evaluate the potential of shock acceleration in the exploded targets to achieve higher proton energies, we employed a CP laser with a larger  $a_0$ . As the laser intensity  $a_0$  increases to 28 ( $3.5 \times 10^{21}$  W/cm<sup>2</sup>) and the peak plasma density  $n_{e,\max}$  is increased to  $16n_c$ , a quasimonoenergetic proton beam of approximately 150 MeV can be reached, as shown in Fig. 4, which approaches the requirement of proton therapy. It should be noted that 800-nm lasers of  $a_0 = 28$  are

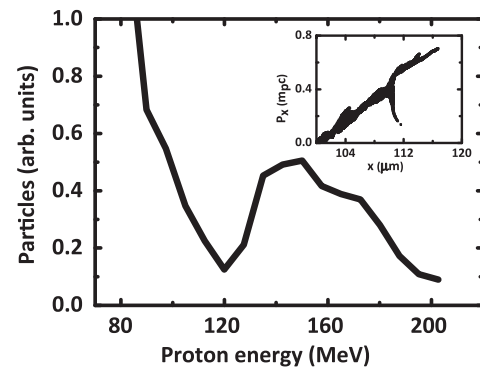


FIG. 4. Simulated proton spectrum obtained from CP laser with  $a_0$  of 28 interacting with an exploded plasma of a peak density  $n_{e,\max} = 16n_c$ . The plasma density profile is identical to that in the  $a_0 = 4$  case. The inset represents the corresponding proton phase space.

achievable given the current developments in laser technology. In view of the very high flux discussed above, this scheme represents an important step for developing high-flux, high-energy, and monoenergetic ion sources. To realize the accurate prediction of higher-energy protons at higher intensity, the experimental conditions should be further optimized (see the Supplemental Material [31] for more information).

In conclusion, we present experimental studies on the ion acceleration from exploded nanofolios irradiated by 800-nm CP lasers, producing quasimonoenergetic proton beams with peak energies up to 9 MeV and high fluxes of  $3 \times 10^{12}$  protons/MeV/sr. 2D PIC simulations reveal that these protons are dominantly accelerated by collisionless shocks, which are efficiently launched by CP lasers. The high-quality proton beams obtained here are urgently required for some medical applications such as proton therapy of skin or eye tumors. Furthermore, this scheme predicts the generation of 150-MeV quasimonoenergetic protons using current laser technology. These results mark a significant step toward future developments in laser-plasma ion accelerators for applications such as cancer therapy that require high-flux ion beams.

This work was supported by the Ministry of Science and Technology of the People's Republic of China (Grant No. 2016YFA0401102), the National Natural Science Foundation of China (Grant No. 11705260), Shanghai Natural Science Foundation (Grant No. 17ZR1434300), and the Strategic Priority Research Program of the Chinese Academy of Sciences (Grant No. XDB16).

---

\*bfshen@mail.shnc.ac.cn

†ruxinli@mail.shnc.ac.cn

- [1] S. Palaniyappan, C. Huang, D. C. Gautier, C. E. Hamilton, M. A. Santiago, C. Kreuzer, A. B. Sefkow, R. C. Shah, and J. C. Fernández, *Nat. Commun.* **6**, 10170 (2015); D. Jung *et al.*, *Phys. Rev. Lett.* **107**, 115002 (2011); A. Henig *et al.*, *Phys. Rev. Lett.* **103**, 045002 (2009).
- [2] A. Yogo *et al.*, *Sci. Rep.* **7**, 42451 (2017); Y. Fukuda *et al.*, *Phys. Rev. Lett.* **103**, 165002 (2009); T. Nakamura, S. V. Bulanov, T. Z. Esirkepov, and M. Kando, *Phys. Rev. Lett.* **105**, 135002 (2010).
- [3] S. V. Bulanov, T. Z. Esirkepov, V. S. Khoroshkov, A. V. Kunetsov, and F. Pegoraro, *Phys. Lett. A* **299**, 240 (2002); M. Borghesi *et al.*, *Phys. Plasmas* **9**, 2214 (2002); M. Roth *et al.*, *Phys. Rev. Lett.* **86**, 436 (2001).
- [4] F. Wagner *et al.*, *Phys. Rev. Lett.* **116**, 205002 (2016); F. Wagner, C. Brabetz, O. Deppert, M. Roth, T. Stöhlker, A. Tauschwitz, A. Tebartz, B. Zielbauer, and V. Bagnoud, *High Power Laser Sci. Eng.* **4**, e45 (2016).
- [5] H. Schwoerer, S. Pfotenhauer, O. Jackel, K. U. Amthor, B. Liesfeld, W. Ziegler, R. Sauerbrey, K. W. D. Ledingham, and T. Esirkepov, *Nature (London)* **439**, 445 (2006).
- [6] B. M. Hegelich, B. J. Albright, J. Cobble, K. Flippo, S. Letzring, M. Paffett, H. Ruhl, J. Schreiber, R. K. Schulze, and J. C. Fernández, *Nature (London)* **439**, 441 (2006).
- [7] T. Esirkepov, M. Borghesi, S. V. Bulanov, G. Mourou, and T. Tajima, *Phys. Rev. Lett.* **92**, 175003 (2004).
- [8] X. Q. Yan, C. Lin, Z. M. Sheng, Z. Y. Guo, B. C. Liu, Y. R. Lu, J. X. Fang, and J. E. Chen, *Phys. Rev. Lett.* **100**, 135003 (2008).
- [9] B. Shen and Z. Xu, *Phys. Rev. E* **64**, 056406 (2001).
- [10] X. Zhang, B. Shen, X. Li, Z. Jin, F. Wang, and M. Wen, *Phys. Plasmas* **14**, 123108 (2007).
- [11] A. Macchi, S. Veghini, and F. Pegoraro, *Phys. Rev. Lett.* **103**, 085003 (2009); C. Scullion *et al.*, *Phys. Rev. Lett.* **119**, 054801 (2017).
- [12] A. Henig *et al.*, *Phys. Rev. Lett.* **103**, 245003 (2009).
- [13] S. Kar *et al.*, *Phys. Rev. Lett.* **109**, 185006 (2012).
- [14] M. Chen, Z.-M. Sheng, Q.-L. Dong, M.-Q. He, Y.-T. Li, M. A. Bari, and J. Zhang, *Phys. Plasmas* **14**, 053102 (2007).
- [15] F. Fiuza, A. Stockem, E. Boella, R. A. Fonseca, L. O. Silva, D. Haberberger, S. Tochitsky, C. Gong, W. B. Mori, and C. Joshi, *Phys. Rev. Lett.* **109**, 215001 (2012).
- [16] Y.-K. Kim, M.-H. Cho, H. S. Song, T. Kang, H. J. Park, M. Y. Jung, and M. S. Hur, *Phys. Rev. E* **92**, 043102 (2015).
- [17] A. Macchi, A. S. Nindrayog, and F. Pegoraro, *Phys. Rev. E* **85**, 046402 (2012); T. V. Liseikina and A. Macchi, *Appl. Phys. Lett.* **91**, 171502 (2007); A. P. L. Robinson, *Phys. Plasmas* **18**, 056701 (2011).
- [18] L. O. Silva, M. Marti, J. R. Davies, R. A. Fonseca, C. Ren, F. S. Tsung, and W. B. Mori, *Phys. Rev. Lett.* **92**, 015002 (2004); A. Stockem Novo, M. C. Kaluza, R. A. Fonseca, and L. O. Silva, *Sci. Rep.* **6**, 29402 (2016).
- [19] M.-Q. He, Q.-L. Dong, Z.-M. Sheng, S.-M. Weng, M. Chen, H.-C. Wu, and J. Zhang, *Phys. Rev. E* **76**, 035402 (2007); L. L. Ji, B. F. Shen, X. M. Zhang, F. C. Wang, Z. Y. Jin, X. M. Li, M. Wen, and J. R. Cary, *Phys. Rev. Lett.* **101**, 164802 (2008); S. Eliezer, J. M. Martinez-Val, Z. Henis, N. Nissim, S. V. Pinhasi, A. Ravid, M. Werdiger, and E. Raicher, *High Power Laser Sci. Eng.* **4**, e25 (2016).
- [20] J. Denavit, *Phys. Rev. Lett.* **69**, 3052 (1992).
- [21] D. W. Forslund and C. R. Shonk, *Phys. Rev. Lett.* **25**, 1699 (1970).
- [22] H. K. Avetissian, A. K. Avetissian, G. F. Mkrtchian, and Kh. V. Sedrakian, *Phys. Rev. ST Accel. Beams* **14**, 101301 (2011); H. K. Avetissian, *Relativistic Nonlinear Electrodynamics: The QED Vacuum and Matter in Super-Strong Radiation Fields* (Springer, New York, 2016).
- [23] C. A. J. Palmer *et al.*, *Phys. Rev. Lett.* **106**, 014801 (2011).
- [24] O. Tresca, N. P. Dover, N. Cook, C. Maharjan, M. N. Polyanskiy, Z. Najmudin, P. Shkolnikov, and I. Pogorelsky, *Phys. Rev. Lett.* **115**, 094802 (2015).
- [25] D. Haberberger, S. Tochitsky, F. Fiuza, C. Gong, R. A. Fonseca, L. O. Silva, W. B. Mori, and C. Joshi, *Nat. Phys.* **8**, 95 (2012).
- [26] H. Zhang *et al.*, *Phys. Plasmas* **22**, 013113 (2015).
- [27] M. Gauthier *et al.*, *Phys. Plasmas* **21**, 013102 (2014).
- [28] M. S. Wei *et al.*, *Phys. Rev. Lett.* **93**, 155003 (2004).
- [29] Y. Chu *et al.*, *Opt. Express* **21**, 29231 (2013).
- [30] Y. Xu, Y. Huang, Y. Li, J. Wang, X. Lu, Y. Leng, R. Li, and Z. Xu, *IEEE J. Quantum Electron.* **48**, 516 (2012).

- [31] See Supplemental Material at <http://link.aps.org/supplemental/10.1103/PhysRevLett.119.164801> for processed method of the proton spectra, laser contrast curve in experiments, energy spectra of carbon ions, and simulated optimization of the incidence angle for the shock acceleration, which includes Ref. [32].
- [32] A. Mančić, J. Fuchs, P. Antici, S. A. Gaillard, and P. Audebert, *Rev. Sci. Instrum.* **79**, 073301 (2008).
- [33] W. P. Wang *et al.*, *Appl. Phys. Lett.* **102**, 224101 (2013).
- [34] A. A. Andreev, S. Steinke, T. Sokollik, M. Schnürer, S. T. Avetsiyan, K. Y. Platonov, and P. V. Nickles, *Phys. Plasmas* **16**, 013103 (2009).